Effect of atomization on surface oxide composition in 316L stainless steel powders for additive manufacturing

(article starts on next page)

RESEARCH ARTICLE

Effect of atomization on surface oxide composition in 316L stainless steel powders for additive manufacturing

Dmitri Riabov[1,3] | Eduard Hryha[1] | Masoud Rashidi[1,2] | Sven Bengtsson[3] |
Lars Nyborg[1]

[1]Industrial and Materials Science, Chalmers University of Technology, Gothenburg, Sweden

[2]Mechanical and Aerospace Engineering, Nanyang Technological University, Singapore

[3]Höganäs AB, Höganäs, Sweden

Correspondence
Dmitri Riabov, Department of Industrial and Materials Science, Chalmers University of Technology, Rännvägen 2A, SE-412 96, Gothenburg, Sweden.
Email: riabov@chalmers.se

The initial oxide state of powder is essential to the robust additive manufacturing of metal components using powder bed fusion processes. However, the variation of the powder surface oxide composition as a function of the atomizing medium is not clear. This work summarizes a detailed surface characterization of three 316L powders, produced using water atomization (WA), vacuum melting inert gas atomization (VIGA), and nitrogen atomization (GA). X-ray photoelectron spectroscopy (XPS) and scanning electron microscopy analyses were combined to characterize the surface state of the powders. The results showed that the surface oxides consisted of a thin ($\sim$4 nm) iron oxide (Fe_2O_3) layer with particulate oxide phases rich in Cr, Mn, and Si, with a varying composition. XPS analysis combined with depth-profiling showed that the VIGA powder had the lowest surface coverage of particulate compounds, followed by the GA powder, whereas the WA powder had the largest fraction of particulate surface oxides. The composition of the oxides was evaluated based on the XPS analysis of the oxide standards. Effects of Ar sputtering on the peak positions of the oxide standards were evaluated with the aim of providing an accurate analysis of the oxide characteristics at different etch depths.

KEYWORDS
316 L, additive manufacturing, atomization, depth profiling, powder, surface oxides, XPS analysis

1 | INTRODUCTION

The field of powder bed additive manufacturing (AM) has recently seen enormous growth, which has been associated with an increase in the number of powder producers, which utilize various melting practices and atomizing media. As of today, most of the produced powder for the powder-based metal AM are vacuum melted and atomized using high purity Ar gas. However, lower-cost powder produced using open air melting and nitrogen gas atomization, or even water atomized grades, can be expected to start making their way into the AM machines as the process becomes more robust and efficient,

opening itself up to more powder grades. This is a viable option for many iron-based alloys, such as stainless steels, engineering steels, and some tool steels. This development, however, is not suitable for highly reactive alloys, such as Ti-alloys.

There are, however, potential drawbacks to using reactive atmospheres during atomization. From the powder metallurgical field, it is known that water-atomized pre-alloyed iron powders with strong oxide forming elements like, Cr and Mn form, besides the dominant Fe-rich thin oxide film, minor amounts of oxide particles.[1-3] If not reduced, these more stable oxsides remain within the consolidated sample.[4-6] Similar correlations have been drawn within the powder

bed fusion AM processes, but these have mostly concerned powders that have been recycled.[7–9] There is hence a lack of published papers focusing on the surface oxide of original powder and the effect of atomizing media on surface chemical composition of the powder in the field of additive manufacturing. There is also lack of knowledge concerning the interaction of the high-power beam (e.g., laser or electron) with powder surfaces covered by oxide species in the actual AM fabrication process. Some research on direct energy deposition has indicated that oxides tend to migrate to open surfaces,[10] whereas other studies have indicated the presence of oxide films on fracture surfaces, causing a premature failure of similarly built alloy IN718.[11,12] These examples emphasize the importance of the surface oxide characteristics of the powder. Thus, before implementing such powders into powder bed systems, it is beneficial to know the surface chemical characteristics of classical gas- and water-atomized grades of iron-base powder in relation to the industry standard of vacuum melting inert gas atomization (VIGA) powder.

Nyborg et al[13] showed that surface characterization techniques, such as X-ray photoelectron spectroscopy (XPS) and Auger electron spectroscopy, are able to provide valuable information concerning the surface state of powder particles. Ion etching, together with mathematical models taking effects such as the angular dependence of the photoelectron flux and the ion sputter yields into account, provided means of performing accurate depth profiles, facilitating the characterization of oxides on various kinds of powder. The early work by Nyborg et al[14,15] showed that the presence of silicon oxide on the surface was minimal for inert gas-atomized ferrous powders, regardless of its content in the alloy. The same author[16,17] later also showed that oxidation of Si could be forced by altering the processing conditions. The relative presence of tetravalent Si would increase as a function of the decreasing partial pressure of oxygen in the atomizing atmosphere and with increasing cooling rate of the metal particles in case of water-atomizing. A recent study[18] that compared gas-atomized to water-atomized powders provided similar observations; no Si oxide was found on a gas-atomized powder, whereas Mn together with Fe and Cr formed the surface oxide instead. Additionally, the content of Mn in the surface oxide layer on the gas-atomized powder was found to increase as the powder particle size decreased, in line with the observations by Norell and Nyborg for a gas-atomized 12% Cr-steel powder.[14] For water atomized powders, the oxidation is governed by the cooling rate, whereby higher degree of selective oxidation is coupled with smaller oxide thickness as cooling rate increases. For gas-atomized powders, O_2 activity in the atomizing gas was shown to be the dominant factor.[2,14,15,17,19]

This study aims to investigate how the atomizing media affect the surface oxide condition of 316L powder variants in comparison to a VIGA powder. As highlighted in a recent review, the powder cost is the second or third largest cost when producing AM parts.[20,21] Therefore, as a means of improving the utilization of additive manufacturing, it is important to highlight the similarities and differences between the powder qualities in ways other than flowability, bulk chemistry, and packing density. The approach involves a dedicated application of surface chemical analysis by means of X-ray photoelectron spectroscopy (XPS) and high-resolution scanning electron microscopy (HR-SEM) combined with X-ray microanalysis. That offers a means of coupling the surface morphology (oxide features, etc.) of powders to the chemical composition of the surface oxide products (given by XPS), thus providing a detailed description of the surface state for powders. It is envisaged that the study provides a basis for the expanded application of normal inert gas-atomized and water-atomized grades of powder in additive manufacturing by powder bed fusion.

2 | MATERIALS AND METHODOLOGY

The scope of this study was to investigate the effects of the atomizing medium on the surface oxide of the powder as well as its bulk chemical composition. Therefore, three grades of stainless steel 316L powder were selected. These were produced using VIGA, air melting and nitrogen gas atomization (GA), and water atomization (WA). The powder materials were provided by Höganäs AB. The VIGA powder was supplied in the 15–45 μm sieve cut, whereas the two other types of powder were supplied in the 20–53 μm sieve cut. The chemical composition of the powder materials was measured by three techniques: inductively coupled plasma–optical emission spectrometry (ICP-OES) using a SPECTRO ARCOS for the majority of alloying elements (e.g., Cr, Ni, and Si), combustion gas analysis for the interstitial elements C, and S using LECO CS844 and hot fusion analysis for the interstitial elements O, and N using LECO ON836.

A general overview of the morphology of oxides found on the particle surfaces was provided by HR-SEM, using a Leo Gemini 1550 instrument, coupled with energy dispersive x-ray spectroscopy (EDS) with an Inca X-Max detector. Further characterization was performed by XPS using a PHI 5500 instrument, followed by transmission electron microscopy (TEM), FEI Tecnai T20, involving prior sample preparation using focused ion beam (FIB), FEI Versa3D, to create milled lift-out from an individual metal particle.

The powder samples were mounted on carbon tape and investigated using an HR-SEM equipped with an in-lens detector and imaged using an accelerating voltage of 15 kV. Special attention was dedicated to the oxide particulate features on the surfaces of the powder. The particulate features were further analyzed using EDS microanalysis, whereby the accelerating voltage was reduced to 5 kV to promote a smaller interaction volume to probe as little of the powder bulk as possible. L_α lines were used for the quantification of Fe, Cr, and Mn.

The PHI 5500 instrument XPS was equipped with monochromatic Al K_α source as well as standard nonchromatized dual Mg K_α/ Al K_α and charge compensation was applied when needed. The spectra were then shifted according to set the position for adventitious C1s peak at 284.8 eV. However, the method of peak alignment using the C1s peak has an inherent error of ± 0.1 eV,[22] with some reports of a variance of up to ±0.3 eV.[23] This means that positioning of characteristic peaks cannot be done with higher precision than this, and peaks closer than the quoted variance cannot either be ascertained.

The beam size was 0.8 mm, thus analyzing a large number of particles simultaneously. This brings the benefit of a statistically reliable result of the surface oxide composition. The generated photoelectrons were collected in a hemispherical analyzer at a pass energy of 23.5 eV using a step size of 0.1 eV. The peaks were fitted using the Multipak software provided by Physical Electronics Inc. Peak shapes were fitted using an asymmetric peak geometry. The background estimation was performed using the iterated Shirley approach within the Multipak software. The binding energy scale of the system was checked prior to the analysis using the peak positions of Au $4f_{7/2}$, Ag $3d_{5/2}$, and Cu $2p_{3/2}$, and the work function was adjusted to provide an Au $4f_{7/2}$ peak position of 83.96 eV. The chemical shift of the compounds was evaluated and compared to high purity standards of known oxides. The peak fitting parameters and positions for the metallic component of $Fe2p_{3/2}$ and $Cr2p_{3/2}$ peaks were obtained through extensive sputtering of the powder sample until no contribution from the oxide states was detected. The peak positions of the oxides were determined by evaluating the position of the peak maximum. Depth profiling was performed by alternating XPS measurements and ion etching. The Ar^+ ions were accelerated at a voltage of 2 kV, with a beam current of 15 mA rastered over an area of 2.5×2.5 mm^2. The resulting etch rate was 3 nm/min as calibrated on an oxidized tantalum foil with a known Ta_2O_5 thickness, and as such, the etch rate was related to Ta_2O_5 units. Quantification of the photoelectron spectra was performed by using the relative sensitivity factors provided by Multipak software. The relative cation content was determined through peak-fitting of the individual elemental peaks to its oxide or elemental state. The peak area of the oxide was then related to the total peak area to determine the fraction of the oxide state. The oxide fraction was then multiplied with quantified data and normalized to provide the relative cation content. Determination of the oxide thicknesses was performed according to the model for metal powder as described by Nyborg,[13] by relating the normalized metallic component of an oxide to the intensity of iron peak as a function of etch depth. For the oxide thickness range and transition metal oxide, the positioning of the oxide/metal interface lies at the point at which the relative metal cation intensity is at 65% of its maximum value, thus depicting the oxide thickness from the etch depth at which this is reached.

For the lift-out, the water atomized powder was mounted onto a carbon tape and introduced into a FIB-SEM. A layer of Pt was deposited onto the surface of a metal particle and milled normal to the bulk of the particle until a lamella was nearly free. An Omniprobe was then attached to the lamella and the last attachment point to the metal particle milled away. The lamella was then attached to a copper grid and subsequently thinned to electron transparency.

The TEM was equipped with a LaB_6 cathode, and it was operated at 200 kV. It was used for capturing bright field images of the metal particle lift-out. The same instrument also has scanning transmission electron capabilities and is capable of EDX analysis. This was used to analyze the composition of the oxides from the lift-out.

3 | RESULTS

3.1 | Chemical analysis of the powders

Table 1 presents the results from the chemical analysis of the analyzed grades of powder. All the powder materials were within the 316L specification. The major differences between them were the contents of silicon and manganese. The WA powder contained the least amount of manganese, while also containing more silicon. The VIGA powder had only traces of silicon. Differences inherent to the different atomizing media were detected in the analysis of the lighter elements, such as the higher nitrogen content in the GA powder and the higher oxygen content in the WA powder, the latter being predominantly a result of the larger specific surface owing to its more rough character for a given size range.

3.2 | SEM and EDS analysis of the surface oxides

The powders were further analyzed using SEM; see Figure 1. Submicron oxide particulate features were found on the powder surfaces of all studied variants. Representative particulate features are highlighted with arrows in Figure 1. The contrast and morphology of the oxide particulate features varied among the different kinds of powder. Even for the same powder, different oxide morphologies were found. An example of this can be seen on the GA powder, in which the surface was decorated with both small bright features and larger dark spherical features. The oxide particulates found on the VIGA powder were seemingly flat, like a splat, with some tendency to form interdendritically on the surfaces. However, the occurrence of the oxide particulates was low, and the surfaces seemed relatively clean. The GA sample had similar features to those found on the VIGA powder. In addition to these features, there were oxide particulates with a darker contrast. These had a hemispherical morphology and appeared to be larger compared to the other oxide particulate features. Such features were not as common as the previously mentioned oxide features. Finally, the water atomized powder surface was also decorated with particulates. The particulates in this case were of a flake morphology, with clearly defined edges. Sometimes, the splats and the darker

TABLE 1 Results from the chemical analysis of the examined powders, in weight percent

| Powder	C	O	N	S	Si	Cr	Ni	Mn	Mo	P	Fe
316L VIGA	0.01	0.028	0.018	0.005	0.05	18.0	14.2	1.4	2.9	0.004	Bal.
316L GA	0.013	0.066	0.14	0.007	0.7	16.5	12.3	1.5	2.5	0.02	Bal.
316L WA	0.033	0.24	0.044	0.005	0.8	16.9	12.7	0.17	2.2	0.02	Bal.
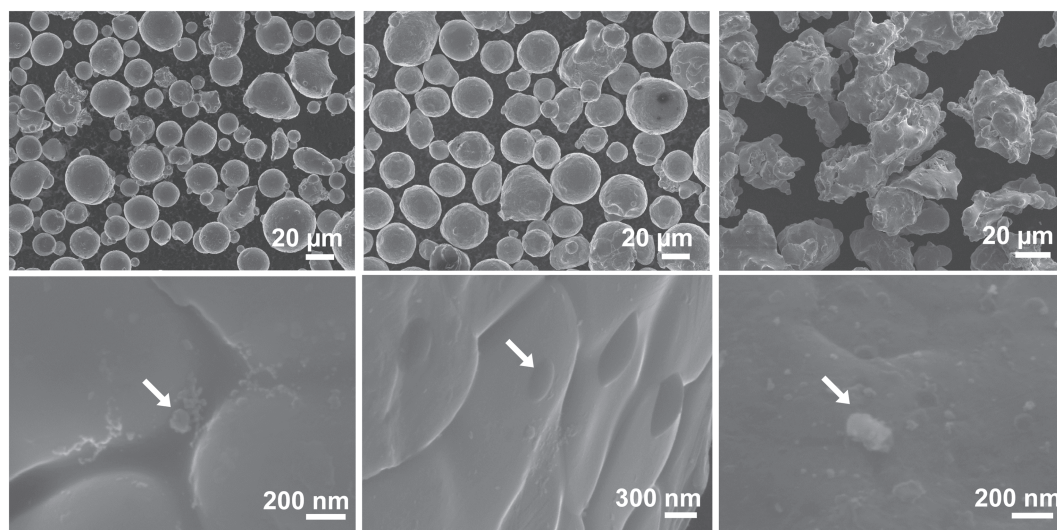
FIGURE 1 SEM micrographs of the powders in overview (top row) and high magnification images of the particulate features (bottom row). Left to right, VIGA, GA, and WA. Dendritic features can be seen on the VIGA and the GA powder

hemispherical objects, similar to the ones observed in the gas atomized powders, were also found on the surfaces of the water atomized grade.

EDS line scans were performed on the particulate features to provide semi-qualitative information concerning their composition. Due to the size of the particulates, the accelerating voltage of the microscope was reduced to 3 (VIGA) and 5 kV to accommodate for this. Figure 2 presents the results of this investigation. The oxide splats found on the VIGA powder were found to be enriched in manganese and chromium, with no detectable signal from silicon. The GA powder, by contrast, had quite strong signal from silicon. The water atomized powder showed similar results to those of the GA powder, with a detectable enrichment in both silicon and chromium. In short, the analysis indicated that oxide particulate features on the surface of gas atomized powder have oxides containing chromium and manganese, with some silicon present in the GA powder. The water atomized powder seemed to have mostly chromium- and silicon-based particulate features.
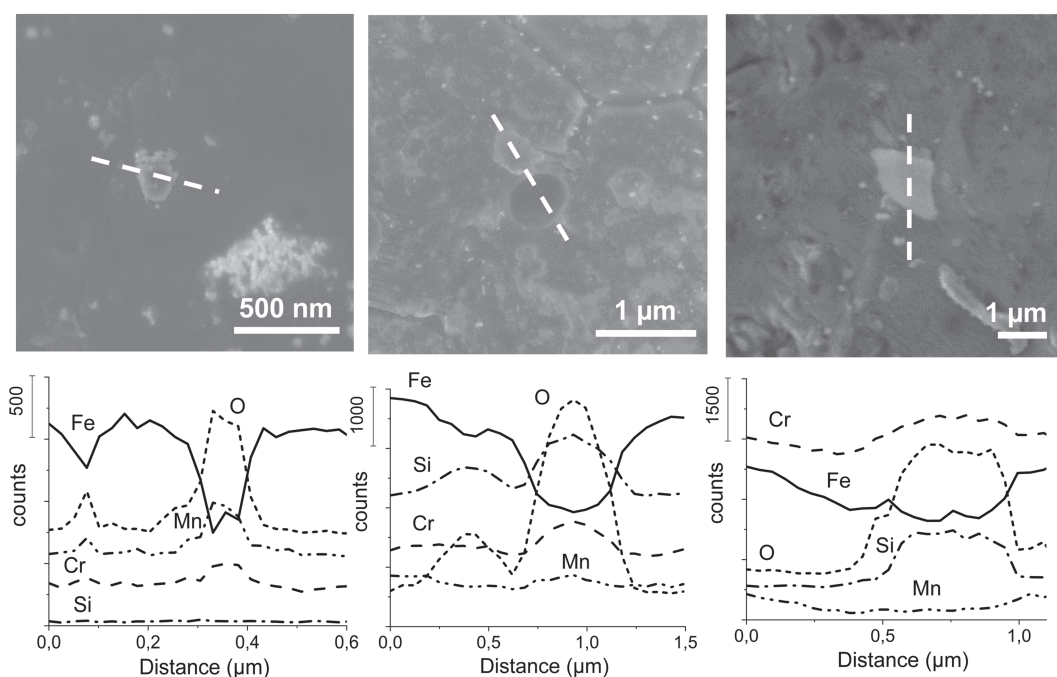
FIGURE 2 High magnification micrographs of particulate compounds and corresponding EDS line scans. From left to right, VIGA, GA, and WA. Spectra are offset for clarity

3.3 | XPS analysis of the powder and the oxide standards

Due to the complexity of oxides on the powder surfaces and the variance in the reference values found in the literature, oxide standards were measured using the same methodology. The high purity oxide samples were Cr_2O_3 (>98.5%, VWR Chemicals), Fe_2O_3 (>99%, Sigma Aldrich), SiO_2 (chemically grown, PHI), MnO_2 (>98%, Mallinckrodt), and Mn_3O_4 (99.99%, Koch-Light). The results can be found below in Table 2. As can be seen, the Fe-strip and Fe_2O_3 show similar peak positions, as the former is supposed to be covered by the native oxide (Fe_2O_3). The Fe $2p_{3/2}$ peak of Fe_2O_3 was additionally fitted by taking into account multiplet splitting, the general multiplet structure according to Biesinger et al[26] was adapted, the results are presented in Table 3.

To assess the influence of Ar ion sputtering on the XPS peak characteristics (peak position, width, and shape), the oxide standards were ion etched to 10 nm nominal depth. The analyses are presented in Figure 3. The Fe_2O_3 and Cr_2O_3 oxides showed extensive broadening and peak shifts. Fe_2O_3 will be partially reduced by ion etching and transforms to its metallic state, as shown from the spectrum recorded after ion etching to 10 nm. This kind of preferential etching is well-known[24] and important to consider when accounting for the oxide composition at larger depths. The Mn oxide did not broaden significantly; however, spectral features typical for MnO (e.g., the satellite peak at ∼646 eV) started to become visible. Thus, significant effects of Ar-etching were evident for the Fe- and Mn-oxide standards and possibly the Cr-oxide standard as well.

The results from the XPS of the powder samples are displayed in Figures 4 and 5, with Table 4 containing a summary of the peaks. Figure 4 shows a detailed scan of the O1s peak in the as-received state of the studied powder, peak locations of SiO_2, Fe_2O_3 and hydroxides are also provided. Figure 5 shows spectra in the as-received state and after ion etching to nominally 3 and 10 nm below the original surface. The spectrum of Fe 2p in the as-received state shows a spin-orbit splitting as well as a satellite feature at 8.5 eV above the main $2p_{3/2}$ peak, located at 710.9 eV for the gas atomized powder samples. The peak was observed at a slightly higher binding energy of 711.1 eV for the WA sample. The Fe $2p_{3/2}$ peaks were fit using the acquired multiplet structure from the Fe_2O_3 standard and

TABLE 3 Fe $2p_{3/2}$ spectral fitting parameters for Fe_2O_3 with respective binding energies, FWHM values, and the area ratios of the peaks relative to the first peak

Peak Number	Peak Position, eV	FWHM, 23.5 eV Pass Energy	Area Ratio
1	709.8	1.5	1
2	710.8	1.7	1
3	711.6	1.7	0.7
4	712.7	1.3	0.3
5	713.7	1.7	0.3

the results of the VIGA and GA powder showed a good fit, hence the Fe oxide is believed to be Fe_2O_3. However, the WA powder did not show a good fit to the multiplet structure, which can be seen in Figure 6, and is therefore likely a mixed Fe oxide. The Fe metal peak was also weakly discerned in the Fe $2p_{3/2}$ peak in all of the samples, showing that the surface oxide was thinner than $3\lambda^{ox}$ in parts of the surface, which for the $2p_{3/2}$-signal from the Fe-oxide would be about 3×1.5 nm = 4.5 nm.[13] After ion etching to 10 nm, only metallic Fe was detected.

Chromium in its oxide state was detected in all samples, with some variation in the peak positions, as can be seen in Table 4. At 10 nm, metallic Cr was found to be dominating as compared to the oxide state for the GA and VIGA powder samples, whereas the spectra of the WA powder still had significant contribution from the oxide state. Intense Mn peaks representing the oxide state were detected in both the VIGA and the GA powder, but absent in the WA powder. The peaks appearing in the Mn-spectra range in the WA powder after ion etching to 3 and 10 nm were due to the Ni Auger emission, which also explained the shift (−0.6 eV) of the peaks in the Mn-spectra range recorded from the GA and VIGA powder samples after ion etching to 10 nm. Nickel appeared in the metallic state at 3 nm for all the powder grades and the Ni Auger peak was calculated to be half the intensity of the Ni $2p_{3/2}$ peak. Silicon was present in its oxide state on the GA, and the WA powders, with traces also detected in the topmost surface of the VIGA powder. The peak at ∼99 eV that appeared at 3 nm and increased in intensity at 10 nm is elemental Si.

To be able to delineate composition gradients on the powder surfaces from potential Ar^+ induced damage, the sputter cleaned

**TABLE 2** XPS binding energies of high purity oxide samples, in eV, corrected using C1s at 284.8 eV

	Met $2p_{3/2}$, eV	FWHM	O1s, eV	FWHM, eV	Reference BE
Fe_2O_3	710.7	3.7	530.3	3.9	711.0–710.8[24–26]
Fe-strip[a]	710.7	3.2	530.1	1.5	710.9[27]
Mn_3O_4	641.5	3.1	529.8	1.2	641.4[28,29]
MnO_2	641.7	2.2	529.3	1.0	641.9–642.7[26,28,29]
Cr_2O_3[b]	576.5	3.3	530.3	2.6	577.1–576.6[30]
SiO_2	103.6	1.5	532.9	1.4	103.6–103.4[31,32]

[a]A 99.99% pure Fe strip was cleaned using 4 kV ion sputtering until no oxide or carbonaceous species could be detected; it was then removed from the XPS chamber and reoxidized briefly in the intro-chamber by venting. The sample was then reintroduced into the chamber and measured.
[b]Measured using an Mg K_α X-ray source.
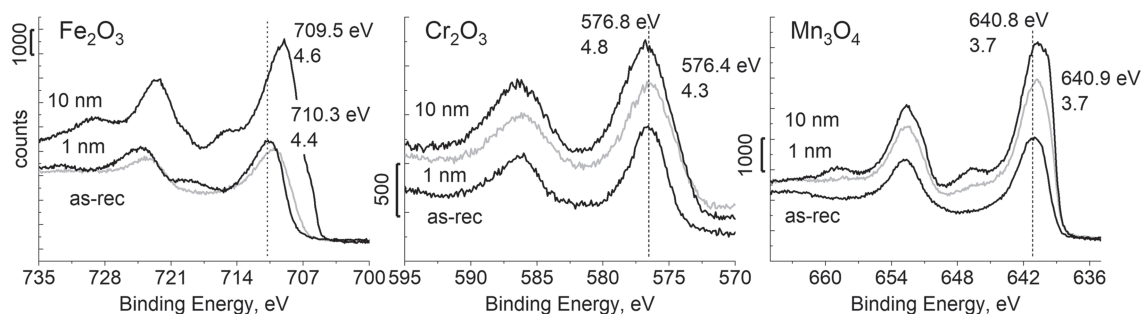
FIGURE 3 XPS spectra of Fe_2O_3, Cr_2O_3, and Mn_3O_4, in the as-received state and after ion etching corresponding to 1 and 10 nm nominal etch depths. The 1 nm spectra are displayed in light gray. The peak positions and FWHM values are provided for the spectra recorded after ion etching. The Cr_2O_3 spectra were measured using an MgK_α source
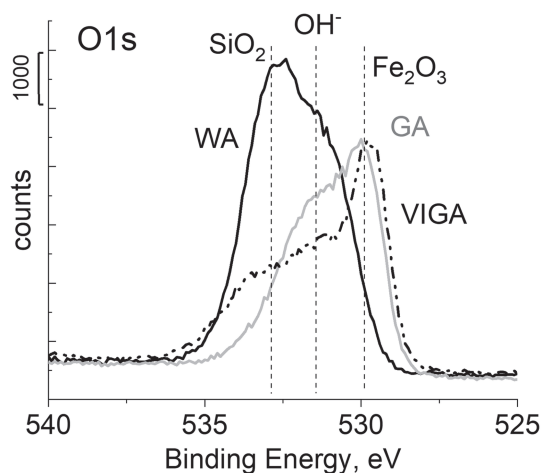
FIGURE 4 Detailed scan of O1s performed on the VIGA, GA, and WA powder in the as-received condition. Location of the hydroxide peak was taken from Biesinger et al[26]

states were compared to the oxide standards, some of which were similarly sputter cleaned; see Table 2 and Figure 3. Several elements in the 316L powders were observed to undergo a chemical shift (see Table 4) relative to the as-received state; specifically, these were Fe, Mn, and Cr. The Fe peak shifted nearly −1 eV, whereas the Cr and Mn peaks had minor shifts, which were consistent with the sputtered standards. Thus, the as-received states of the powder were used to assess the proper state of the oxide species, as the observed shift due to Ar ion sputter damage cannot be disregarded.

3.4 | XPS depth profiling of the powder samples

Successive XPS analyses and ion etching was employed down to a depth of 100 nm for all studied powder materials to depict the homogeneity and thickness of the surface oxide. Figure 7 presents the findings, in which the apparent concentration of elements, independent of the chemical state, are plotted as a function of the nominal etch depth. It should be noted here that the representation in Figure 7 is semiquantitative, as oxide and metal states are not differentiated in

the analyses. Still, quantification after extended ion etching seemed to correlate to the measured compositions in Table 1. Additionally, the measured oxygen content after 1 nm of ion etching, at which the adventitious carbon was removed, was found to be around 65 at.%. This approximately corresponds to the content of oxygen in oxides of M_2O_3 or MO_2 type, as would be the case for Fe_2O_3 and Cr_2O_3, as well as for SiO_2 and MnO_2, respectively. Hence, it is supposed that the sensitivity factors were within acceptable values. To highlight the preferential elemental enrichment in compounds on the surface (top 100 nm), an enrichment factor was calculated and plotted; see Figure 8. The enrichment factor (EF) is a ratio of the quantified element to the measured bulk powder content in atomic percentage (e.g., $EF_{Cr} = Cr_{surface}/Cr_{bulk}$). A strong enrichment of Si and Mn was present for the gas atomized powders, although Si was only present in a presumed monolayer on the VIGA powder. The water atomized powder, however, was only enriched in Si.

Although the enrichment factor highlights the element enrichment at the surfaces, it underestimates the presence of elements that are also abundant in the alloy matrix (e.g., Fe and Cr). In addition, enrichment factors do not provide information concerning the chemical state of a specific element. To properly assess the state and quantity of these elements, each of the spectra from the narrow scans were deconvoluted and related to the total intensity of the peak. These data were normalized and can be found in Figure 9. Here, the relative cation content is displayed as a function of the etch depth. To read the figure correctly, it is important to note that the data in Figure 9 does not take into account that the oxide is gradually removed as the surface is ion etched, but it can be viewed as a means of telling which oxide species extend to greater depth than others. For the VIGA powder, the top 3 nm of the surface oxide is dominated by Fe and Mn, at relative cation concentrations of 50 and 35 at. %, respectively. The cation concentration of Mn decreased rapidly after initial 2 nm of ion etching, stabilizing at 20 at. %. For the GA powder, most of the cations were found in a nearly equiatomic ratio in the as-received state, whereas after 5 nm, Cr cations were dominating. In the range of 1–3 nm, the amount of Mn and Si cations decreased rapidly, and Fe becomes the dominant cation. The WA powder showed a high relative content of Si cations throughout the profile. Chromium was found to increase in cation concentration up to 5 nm, where it
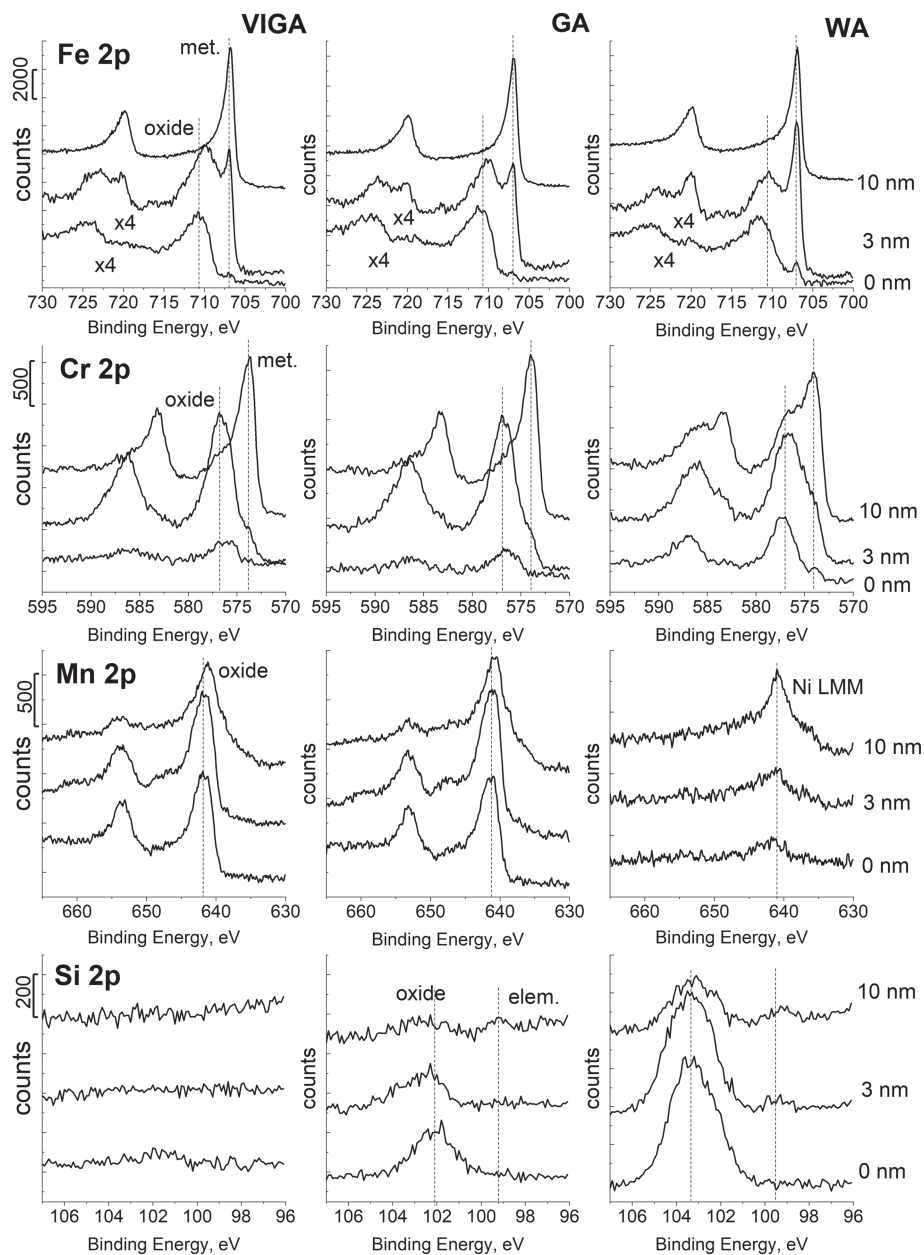
FIGURE 5 Detailed scans of Fe 2p, Cr 2p, Mn 2p, and Si 2p performed on the three studied powders. From left to right, VIGA, GA, and WA

TABLE 4 XPS binding energies in eV, measured on as-received powder surface and after etching 1 nm, corrected using adventitious carbon to 284.8 eV

	Fe2p$_{3/2}$	Cr2p$_{3/2}$	Mn2p$_{3/2}$	Si2p	O1s
VIGA	710.9 ± 0.1	576.3 ± 0.1	641.3 ± 0.2	102.0 ± 0.1	529.8 ± 0.1
VIGA 1 nm	710.0	576.7	641.0	<LOD	530.2
GA	710.9 ± 0.1	576.6 ± 0.1	641.8 ± 0.3	102.1 ± 0.1	530.0 ± 0.1
GA 1 nm	709.9	576.6	641.5	102.1	530.2
WA	711.1 ± 0.1	576.9 ± 0.2	<LOD	102.8 ± 0.1	532.0 ± 0.1
WA 1 nm	710.4	576.5	<LOD	103.0	532.5

Note. LOD indicates that the peak was under the limit of detection. Peak positions after 1 nm etching are provided to show the peak shift relative to the as-received state.

FIGURE 6 Spectral fit of the Fe $2p_{3/2}$ peaks of the VIGA, GA and WA powder using the multiplet structure described in Table 3, the fit envelope is drawn in red
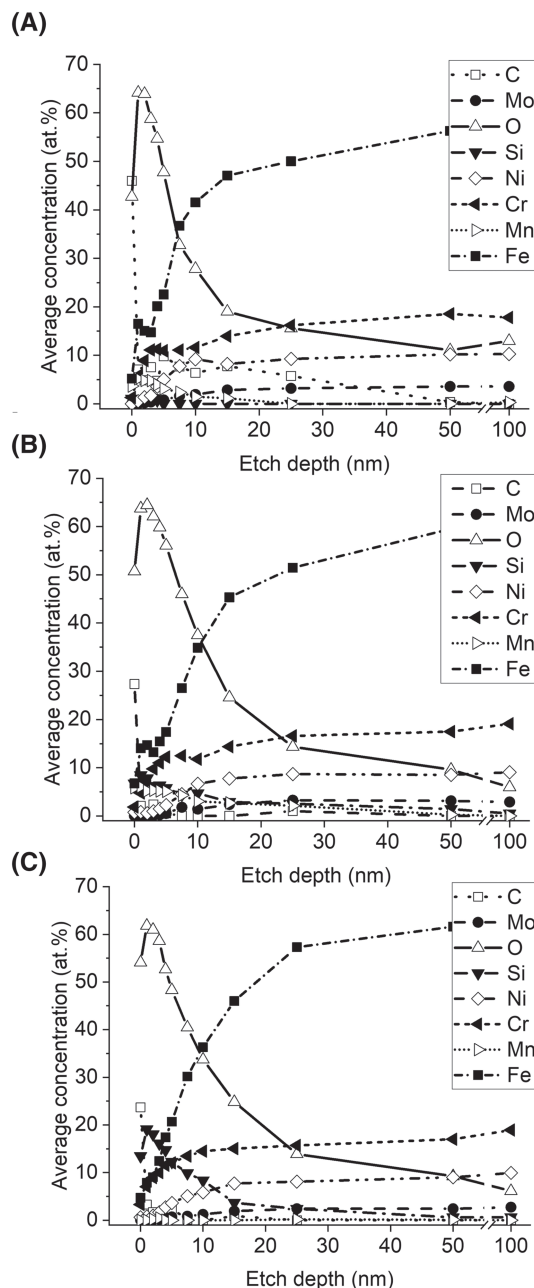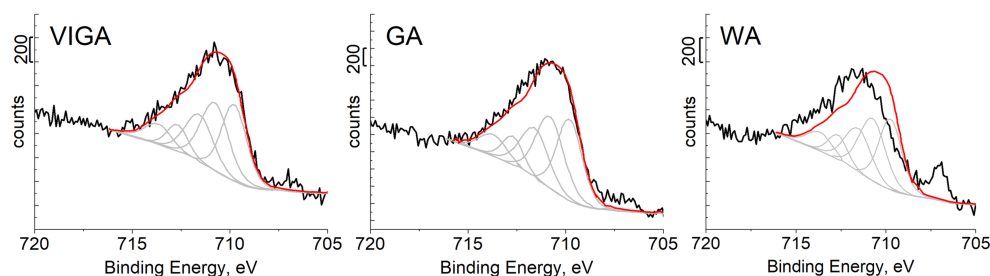
FIGURE 7 Depth profiles and quantification of the present elements for the studied powders: (A) VIGA, (B) GA, and (C) WA

stabilized at around 35 at. %. In all of the observed profiles, the top surface was found to be depleted in Cr. Manganese, by contrast, was found to be removed rapidly with ion etching.

Another benefit of depth profiling using XPS is that it provides the possibility of evaluating the thickness of the surface oxide compounds. When analyzing the oxygen profile from the XPS depth profiling, Figures 7 and 9, the Fe, Cr, Mn, and Si peaks, and the HR-SEM observations in Figure 2, it is evident that the powder surfaces are covered by a heterogeneous oxide layer consisting of an Fe-oxide layer and particulate oxide features, comprised of stable oxides, as also reported in the literature.[1–3] As the particulates cover a small area fraction of the powder, most of the remaining surface was covered by a thin iron oxide that did not resolve in the HR-SEM. The evaluation of the oxide layer thickness using the relative oxygen content of 50% gives a value of 5.6, 6.5, and 7.8 nm for the VIGA, GA, and WA powder samples, respectively. These values represent composite values for the gas atomized powder samples[33] and are connected to the contribution from the fine oxide particulates besides the Fe-oxide layer.[1,3]

The apparent thickness of the iron oxide layer was calculated from the metallic component of the Fe $2p_{3/2}$ peak as function of etch depth. Figure 9D presents the normalized iron intensities as a function of the etch depth for the studied powder samples. The WA powder had the thinnest apparent Fe oxide layer of 3.1 nm among all of the studied powder materials. Meanwhile, the gas atomized powder samples had a similar surface oxide layer thicknesses of 4.1 and 4.0 nm for the VIGA and GA powder, respectively. The discrepancy between these values and the values calculated using the relative intensity of oxygen is due to the influence of the particulate compounds, as described above. Thus, larger difference between the values determined for Figures 5 and 9D indicates that the coverage of particulate compounds is larger relative to the iron oxide layer, and vice versa.

3.5 | TEM of FIB lift-out

An FIB lamella for TEM studies was prepared from the WA powder to verify and delineate the results acquired from the XPS measurements. To alleviate the Ga^+ induced amorphization and damage, and to increase the chances of extracting an actual surface oxide, a thicker oxide particulate was chosen for the lift-out, see Figure 10. Figure 11 presents a TEM bright field composite image of the lift-out; the arrows indicate (1) the Pt layer, which was deposited on top of the powder particle (dark grey contrast), and (2) the oxide particulate, which was the target for the lift-out. EDS spectra of the particulate compound were recorded, in which it was found that the oxide contained roughly
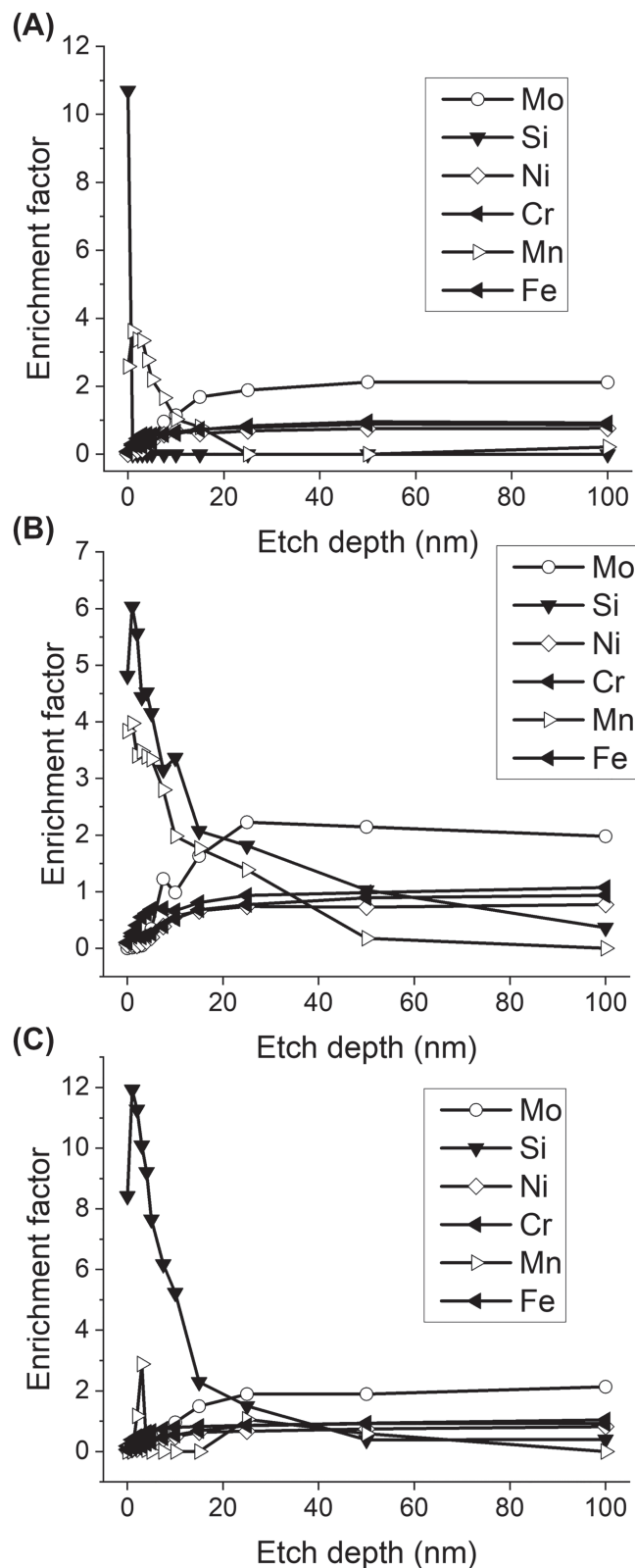
FIGURE 8 Enrichment factors of (A) VIGA, (B) GA, and (C) WA

equimolar amounts of Cr and Si; see Figure 11C. The particulate was found to be heterogenous, with smaller nanometric spherical particulates within the thicker layer; see Figure 11B. The smaller particulates were found to be enriched in Si (not shown here). It appears that the

oxide had grown inwards into the powder particle, as it extends beyond the powder particle surface, which is outlined with a dashed white line in Figure 11.

High resolution TEM was used to investigate the interface between the metal and the oxide particulate. Figure 12 shows the interface between the particulate and the matrix, and the oxide particulate was found to be amorphous; see fast Fourier transformations (FFT) insets.

4 | DISCUSSION

The results from the SEM imaging and the XPS measurements accord with the common consensus of the surface oxide characteristics in case of both inert gas atomized powder and water atomized powder of stainless steel. Both kinds of inert gas-atomized powder (VIGA and GA) had particulate compounds rich in Mn and Cr cations; the GA did, however, has a significant amount of oxidized Si present (>6 at.%), which has not been previously reported. This suggests that the atomizing gas was very low on residual O_2, forcing elements with the highest oxygen affinity, in this case Si, to oxidize.[16]

The peak fitting and deconvolution to define specific chemical states proved to be more difficult, as some shifting of the peak positions was observed, as well as the shift of C1s, which was used as a reference. The two inert gas atomized samples displayed many similarities. No surface enrichment of nitrogen or nitride formation was detected for the GA powder; hence, most of nitrogen is in solid solution within the austenite and was therefore not detected. Small differences were observed for the Cr $2p_{3/2}$, Mn $2p_{3/2}$, and O1s peak positions. Proper Mn identification was difficult due to the spread in measured values and the similarity in peak positions of the reference Mn oxide samples. It is also a fact that different Mn-oxides do not show distinctly different XPS peak positions, whereas the satellite at 6 eV binding energy is significant for MnO. The Cr $2p_{3/2}$ peak of the VIGA powder was believed to be a Cr oxide. It had, however, shifted to slightly lower binding energy peak position (576.3 eV) in the as-received state compared to the standard and the GA powder, and it was found to shift to the peak position of the oxide standard after sputter cleaning of the powder surface (1 nm). The peak shift is believed to be connected to the low intensity and the large width of the peak as well as the C1s peak position, which was used as a reference. The Si 2p positions of VIGA and GA matched those of silicates as reported in literature.[34,35] However, other components of the silicate phase could not be clearly differentiated.

With the WA powder, there was a considerable shift in the C1s peak. Initially believed to be a case of sample charging, upon closer spectra analysis, the early notions of charging were disregarded. Within the Fe 2p spectra of the WA powder, a discernible metal component was present at 706.9 eV in the uncorrected spectra. If shifted for adventitious carbon, the same peak would locate at 706.5 eV, which would not be consistent with the data collected in this study. If left as is, the measured peak position of Fe 2p and Cr 2p would correlate better to the positions of hydroxides of both

**FIGURE 9** XPS depth profile of cation concentrations of (A) VIGA, (B) GA, and (C) WA; (D) Fe oxide layer thickness determination
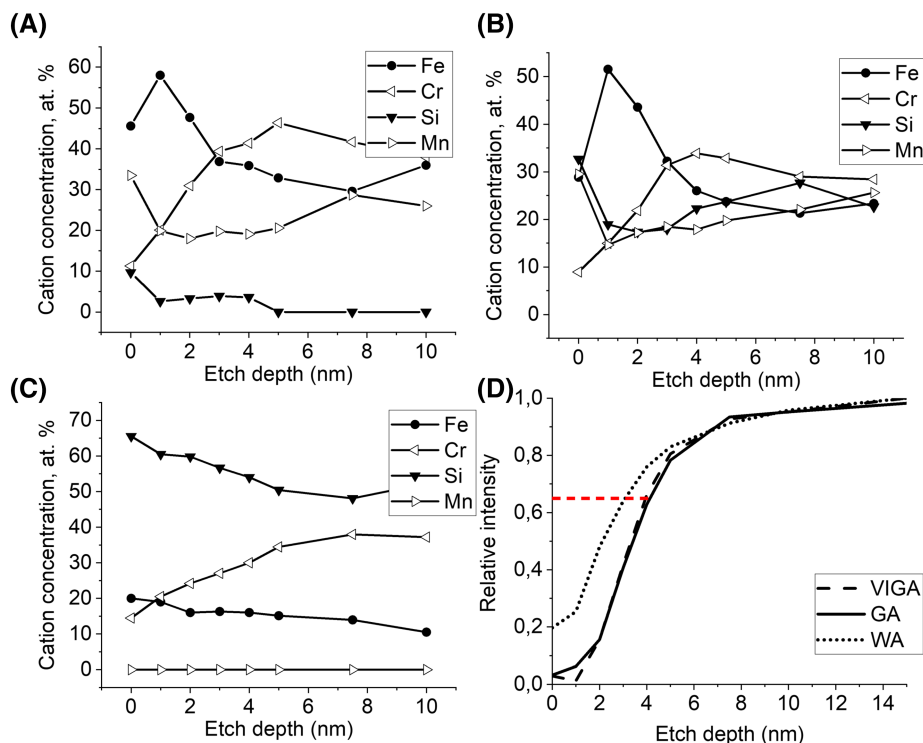
FIGURE 10 SEM images of a WA powder particle prior to Pt deposition (left) and with the Pt layer (right)
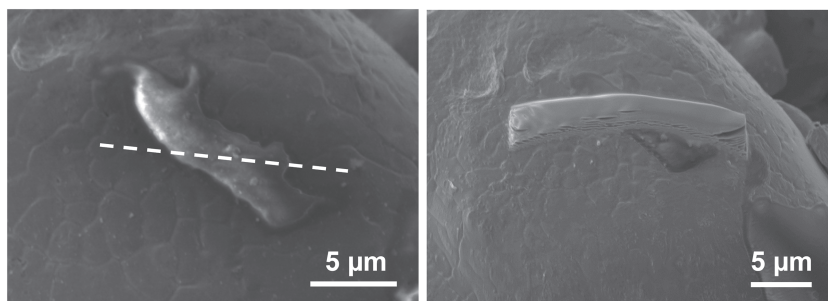
FIGURE 11 (A) Stitched bright-field TEM micrograph of the lamella sampled from the WA powder surface; arrows indicate (1) the Pt layer and, underneath it, (2) a thicker oxide particulate. The dashed box indicates the area in which Figure 12 was taken. The image is mirrored relative to Figure 10. (B) Higher magnification of the internal oxides within the particulate. (C) an EDX spectrum of the particulate compound, the Cu signal comes from the Cu grid and is excluded in the quantification

Element	At. %
O(K)	60
Si(K)	18
Cr(K)	16
Mn(K)	3
Fe(K)	1
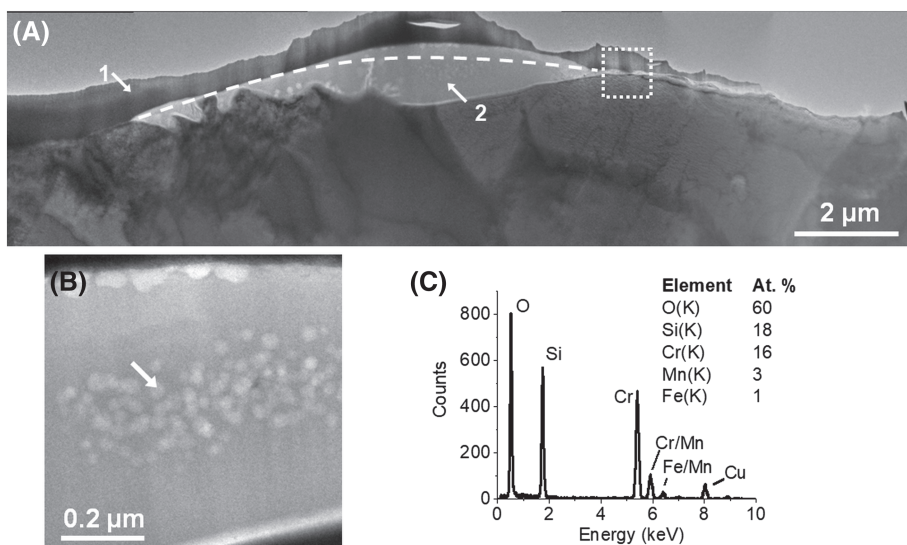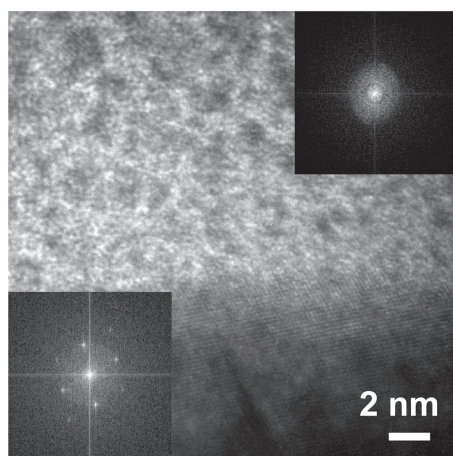
FIGURE 12 Interface between the oxide particulate and the metal of the powder particle, with two FFT insets showing the crystalline metallic matrix and the amorphous oxide layer

elements (located at higher BE). Further evidence regarding the variance of the C1s peak was measured during oxide growth experiments on an Fe plate. Because the exposure time to air was so brief, the metallic peaks were still well discernible and were used for correct peak positioning. This positioned the C1s peak at 285.1 eV. Miller et al[22] reported a variance of the C1s position due to reactions of carbonaceous species, mainly CO and CO_2, with clean Fe surfaces. The same study also reported a high BE subpeak, at $\sim$285.5 eV, compared to the main C1s peak; this was the major peak in the WA powder. Other studies[36,37] also reported similar tendencies in other metals, causing a shift in the C1s signal. In a review, Swift[38] also cautions on the use of C1s signal for spectra positioning. Based on the findings and the data found in literature, it is believed that the C1s signal is shifted relative to the commonly used position of 284.8 eV and can therefore lead to inaccurate peak identification for the studied materials. A more reliable method is to use some other reference peak, for example, a known metallic peak, if present. The problem is that metallic components are seldom present on powder surfaces in the as-received state. Using the O1s peak requires the user to already be familiar with the oxide system of the analyzed surface to provide a reliable method for spectra positioning. Thus, the C1s signal perhaps remains the easiest method of spectra positioning when analyzing unfamiliar surfaces. However, as seen in this study, it should not be used without close scrutiny.

Provided by TEM, the results regarding the particulate chemistry correlated closely with the quantification done by XPS. The observed oxide particulate heterogeneities have been suggested before[1] but for low-alloyed and annealed water atomized steel powder. Thus, observations varied from those in this study, the results of which clearly indicate that oxide inclusions are nucleating within the larger amorphous particulate feature itself and are indicative of inherent oxide heterogeneity.

Putting everything into the context of AM, the crucial aspect is to determine whether differences in the surface oxide composition are significant between the different atomization methods and how

these differences could potentially affect the processability of such powders in the case of powder bed fusion processes. The difference between the VIGA powder and the GA powder was considered minimal, particulate coverage, and the amount of oxidized Si were the sole differences. Previous research[39] shows that Mn can readily combine with Si to form low-temperature melting silicate phases. The presence of a Mn-silicate on the top surface would provide an explanation for the Si and Mn surface enrichments found on the gas atomized powder. However, the presence of such phase on a 316L powder surface in similar amounts was found not to be detrimental in the case of L-PBF, as such particulates were found as fine inclusions with a similar or identical composition inside the dimples on the fracture surface, with no registered impact on mechanical properties due to their low content in the material.[40] Similarly, no nitrogen-rich inclusions were found within the dimples of the same study, hence the nitrogen remains in solid solution throughout L-PBF processing.[40] Furthermore, in SiO_2-Cr_2O_3 systems, such low melting phases do not form, and thus, the oxidation products found on the WA sample would not pose a risk.

5 | CONCLUSIONS

This work has examined the effect of the atomizing medium on the surface oxide state of three different kinds of 316L powder. These grades were produced using vacuum induction melting inert gas atomization, conventional nitrogen gas atomization, and water atomization. A detailed surface characterization was performed using high resolution SEM imaging coupled with XPS analysis. The results were further verified using TEM investigations of a lift-out from a WA powder particle. The results indicated a significant effect of the atomizing media on the surface oxide chemistry and can be summarized as follows:

- The VIGA powder was covered by a homogeneous Fe_2O_3 oxide layer with a thickness of about 4 nm. Submicron oxide particulates rich in Cr and Mn cations with traces of a Si cation were detected, covering a minor part of the surface (below 5%).
- The GA powder has similar surface oxide composition to the VIGA powder, with the iron oxide layer having a thickness of about 4 nm. Particulate oxide features were found to be rich in Cr, Mn, and Si cations as well. The fraction and size of the oxide particulates covering the powder surface is higher than in the case of VIGA powder, evaluated to be up to 5%.
- The WA powder surface is characterized by a higher fraction of particulates rich in Cr- and Si-rich oxides, with a thin Fe-oxide layer of about 3 nm covering a minor part of the surface. The surface coverage of particulate oxides was hence significantly higher than for the two gas atomized powder grades.
- The XPS C1s peak measured on powder surfaces was found to be shifting significantly relative to the commonly used value of 284.8 eV for adventitious carbon. This makes energy referencing using C1s signal for metal powder ambiguous when needed, and its use must be closely scrutinized.

- The TEM analysis of the lift-out confirmed the findings of the XPS and showed that oxide particulates are rich in Cr and Si. In addition, the nucleation of the fine oxides inside oxide particulates was shown.

ACKNOWLEDGEMENTS

ORCID

Dmitri Riabov https://orcid.org/0000-0003-3179-6403
Eduard Hryha https://orcid.org/0000-0002-4579-1710
Sven Bengtsson https://orcid.org/0000-0002-1397-8599
Lars Nyborg https://orcid.org/0000-0002-1726-5529

REFERENCES

1. Chasoglou D, Hryha E, Norell M, Nyborg L. Characterization of surface oxides on water-atomized steel powder by XPS/AES depth profiling and nano-scale lateral surface analysis. *Appl Surf Sci*. 2013; 268:496-506. https://doi.org/10.1016/j.apsusc.2012.12.155

2. Tunberg T, Nyborg L. Surface reactions during water atomisation and sintering of austenitic stainless steel powder. *Powder Metall*. 1995;38 (2):120-130. https://doi.org/10.1179/pom.1995.38.2.120

3. Hryha E, Gierl C, Nyborg L, Danninger H, Dudrova E. Surface composition of the steel powders pre-alloyed with manganese. *Appl Surf Sci*. 2010;256(12):3946-3961. https://doi.org/10.1016/j.apsusc.2010.01.055

4. Gruber H, Karimi P, Hryha E, Nyborg L. Effect of powder recycling on the fracture behavior of electron beam melted alloy 718. *Powder Metall Prog*. 2018;18(1):40–48. https://content.sciendo.com/view/journals/pmp/18/1/article-p40.xml

5. Cooper AJ, Cooper NI, Dhers J, Sherry AH. Effect of oxygen content upon the microstructural and mechanical properties of type 316L austenitic stainless steel manufactured by hot Isostatic pressing. *Metall Mater Trans A*. 2016;47(9):4467-4475. https://doi.org/10.1007/s11661-016-3612-6

6. Rao GA, Srinivas M, Sarma DS. Effect of oxygen content of powder on microstructure and mechanical properties of hot isostatically pressed superalloy Inconel 718. *Mater Sci Eng A*. 2006;435:84-99. https://doi.org/10.1016/j.msea.2006.07.053

7. Gruber H, Henriksson M, Hryha E, Nyborg L. Effect of powder recycling in electron beam melting on the surface chemistry of alloy 718 powder. *Metall Mater Trans A*. 2019;50(9):4410-4422. https://doi.org/10.1007/s11661-019-05333-7

8. Popov VV, Katz-Demyanetz A, Garkun A, Bamberger M. The effect of powder recycling on the mechanical properties and microstructure of electron beam melted Ti-6Al-4 V specimens. *Addit Manuf*. 2018;22:834-843. https://doi.org/10.1016/j.addma.2018.06.003

9. Galicki D, List F, Babu SS, et al. Localized changes of stainless steel powder characteristics during selective laser melting additive manufacturing. *Metall Mater Trans Phys Metall Mater Sci*. 2019;50(3):1582-1605. https://doi.org/10.1007/s11661-018-5072-7

10. Xu X, Ding J, Ganguly S, Diao C, Williams S. Oxide accumulation effects on wire + arc layer-by-layer additive manufacture process. *J Mater Process Technol*. 2018;252:739-750. https://doi.org/10.1016/j.jmatprotec.2017.10.030

11. Zhang YN, Cao X, Wanjara P, Medraj M. Oxide films in laser additive manufactured Inconel 718. *Acta Mater*. 2013;61(17):6562-6576. https://doi.org/10.1016/j.actamat.2013.07.039

12. Campbell J, Tiryakioğlu M. Bifilm defects in Ni-based alloy castings. *Metall Mater Trans B*. 2012;43(4):902-914. https://doi.org/10.1007/s11663-012-9655-1

13. Nyborg L, Nylund A, Olefjord I. Thickness determination of oxide layers on spherically-shaped metal powders by ESCA. *Surf Interface Anal*. 1988;12(2):110-114. https://doi.org/10.1002/sia.740120209

14. Nyborg L, Norell M, Olefjord I. Surface studies of powder metallurgical stainless steel. *Surf Interface Anal*. 1992;19(1–12):607-614. https://doi.org/10.1002/sia.7401901113

15. Olefjord I, Nyborg L. Surface analysis of gas atomized Ferritic steel powder. *Powder Metall*. 1985;28(4):237-243. https://doi.org/10.1179/pom.1985.28.4.237

16. Nyborg L, Olefjord I. Surface analysis of REP-atomized martensitic steel powder. *Powder Met Int*. 1988;20(2):11-16.

17. Nyborg I, Tunberg T, Wang PX. Surface product formation during water atomization and sintering of austenitic stainless steel powder. *Met Powder Rep*. 1990;45(11):750-753. https://doi.org/10.1016/0026-0657(90)90459-T

18. Hedberg Y, Norell M, Hedberg J, Szakálos P, Linhardt P, Odnevall WI. Surface characterisation of fine inert gas and water atomised stainless steel 316L powders: formation of thermodynamically unstable surface oxide phases. *Powder Metall*. 2013;56(2):158-163. https://doi.org/10.1179/1743290112Y.0000000041

19. Nyborg L, Olefjord I. Surface analysis of PM martensitic steel before and after consolidation: part 1: surface analysis of powder. *Powder Metall*. 1988;31(1):33-39. https://doi.org/10.1179/pom.1988.31.1.33

20. Campbell I, Diegel O, Kowen J, Wohlers T. Wohlers Report 2018: 3D Printing and Additive Manufacturing State of the Industry: Annual Worldwide Progress Report. Wohlers Associates; 2018.

21. Vock S, Klöden B, Kirchner A, Weißgärber T, Kieback B. Powders for powder bed fusion: a review. *Prog Addit Manuf*. 2019;4(4):383-397. https://doi.org/10.1007/s40964-019-00078-6

22. Miller DJ, Biesinger MC, McIntyre NS. Interactions of CO_2 and CO at fractional atmosphere pressures with iron and iron oxide surfaces: one possible mechanism for surface contamination? *Surf Interface Anal*. 2002;33(4):299-305. https://doi.org/10.1002/sia.1188

23. Hochella MF, Brown GE. Aspects of silicate surface and bulk structure analysis using X-ray photoelectron spectroscopy (XPS). *Geochim Cosmochim Acta*. 1988;52(6):1641-1648. https://doi.org/10.1016/0016-7037(88)90232-3

24. McIntyre NS, Zetaruk DG. X-ray photoelectron spectroscopic studies of iron oxides. *Anal Chem*. 1977;49(11):1521-1529. https://doi.org/10.1021/ac50019a016

25. Grosvenor AP, Kobe BA, Biesinger MC, McIntyre NS. Investigation of multiplet splitting of Fe 2p XPS spectra and bonding in iron compounds. *Surf Interface Anal*. 2004;36(12):1564-1574. https://doi.org/10.1002/sia.1984

26. Biesinger MC, Payne BP, Grosvenor AP, Lau LWM, Gerson AR, Smart RSC. Resolving surface chemical states in XPS analysis of first row transition metals, oxides and hydroxides: Cr, Mn, Fe, Co and Ni. *Appl Surf Sci*. 2011;257(7):2717-2730. https://doi.org/10.1016/j.apsusc.2010.10.051

27. Suzuki S, Ishikawa Y, Isshiki M, Waseda Y. Native oxide layers formed on the surface of ultra high-purity iron and copper investigated by angle resolved XPS. *Mater Trans JIM*. 1997;38(11):1004-1009. https://doi.org/10.2320/matertrans1989.38.1004

28. Oku M, Hirokawa K, Ikeda S. X-ray photoelectron spectroscopy of manganese—oxygen systems. *J Electron Spectrosc Relat Phenom*. 1975;7(5):465-473. https://doi.org/10.1016/0368-2048(75)85010-9

29. Ilton ES, Post JE, Heaney PJ, Ling FT, Kerisit SN. XPS determination of Mn oxidation states in Mn (hydr)oxides. *Appl Surf Sci*. 2016;366: 475-485. https://doi.org/10.1016/j.apsusc.2015.12.159

30. Biesinger MC, Brown C, Mycroft JR, Davidson RD, McIntyre NS. X-ray photoelectron spectroscopy studies of chromium compounds.

Surf Interface Anal. 2004;36(12):1550-1563. https://doi.org/10.1002/sia.1983

31. Zakaznova-Herzog VP, Nesbitt HW, Bancroft GM, Tse JS, Gao X, Skinner W. High-resolution valence-band XPS spectra of the nonconductors quartz and olivine. *Phys Rev B.* 2005;72(20): 205113. https://doi.org/10.1103/PhysRevB.72.205113

32. Wagner CD, Riggs WM, Davis LE, Moulder JF, Mullenberg GE. *Handbook of X-Ray Photoelectron Spectroscopy*. Eden Prairie, Minnesota: Perkin- Elmer Corporation; 1995.

33. Zumsande K, Weddeling A, Hryha E, et al. Characterization of the surface of Fe–19Mn–18Cr–C–N during heat treatment in a high vacuum—an XPS study. *Mater Charact.* 2012;71:66-76. https://doi.org/10.1016/j.matchar.2012.06.002

34. Adams I, Thomas J, Bancroft G. An ESCA study of silicate minerals. *Earth Planet Sci Lett.* 1972;16(3):429-432. https://doi.org/10.1016/0012-821X(72)90163-X

35. Grosvenor AP, Bellhouse EM, Korinek A, Bugnet M, McDermid JR. XPS and EELS characterization of Mn_2SiO_4, $MnSiO_3$ and $MnAl_2O_4$. *Appl Surf Sci.* 2016;379:242-248. https://doi.org/10.1016/j.apsusc.2016.03.235

36. Browne VM, Carley AF, Copperthwaite RG, Davies PR, Moser EM, Roberts MW. Activation of carbon dioxide at bismuth, gold and copper surfaces. *Appl Surf Sci.* 1991;47(4):375-379. https://doi.org/10.1016/0169-4332(91)90091-W

37. Carley AF, Gallagher DE, Roberts MW. Activation of carbon dioxide at low temperatures at aluminium surfaces. *Surf Sci.* 1987;183(1): L263-L268. https://doi.org/10.1016/S0039-6028(87)80324-2

38. Swift P. Adventitious carbon—the panacea for energy referencing? *Surf Interface Anal.* 1982;4(2):47-51. https://doi.org/10.1002/sia.740040204

39. Tanahashi M, Furuta N, Yamauchi C, Fujisawa T. Phase equilibria of the MnO-SiO_2-CrOx system at 1873 K under controlled oxygen partial pressure. *ISIJ Int.* 2001;41(11):1309-1315. https://doi.org/10.2355/isijinternational.41.1309

40. Pauzon C, Hryha E, Forêt P, Nyborg L. Effect of argon and nitrogen atmospheres on the properties of stainless steel 316L parts produced by laser-powder bed fusion. *Mater Des.* 2019;179: 107873. https://doi.org/10.1016/j.matdes.2019.107873